Full Length Article

Effect of wire and arc additive manufacturing (WAAM) process parameters on bead geometry and microstructure

Malcolm Dinovitzer, Xiaohu Chen, Jeremy Laliberte*, Xiao Huang, Hanspeter Frei

Mechanical and Aerospace Engineering Carleton University, 1125 Colonel By Dr Ottawa, ON Canada K1S5B6, United States

ABSTRACT

This paper discusses the effects of process parameters in TIG based WAAM for specimens created using Hastelloy X alloy (Haynes International) welding wire and 304 stainless-steel plate as the substrate. The Taguchi method and ANOVA were used to determine the effects of travel speed, wire feed rate, current, and argon flow rate on the responses including bead shape and size, bead roughness, oxidation levels, melt through depth, and the microstructure. Travel speed and current were found to have the largest effect on the responses. Increasing travel speed or decreasing current caused a decrease in melt through depth and an increase in roughness. Printing strategies were tested using specimens of multiple layers and no significant difference was found between printing layers in the same direction and printing layers in alternating directions. No observable interface between the layers was present suggesting a complete fusion between layers with no oxidation. Three distinct zones were identified within the three- and eight-layer samples. The zones were characterized by the size and distribution of the molybdenum carbide formations within the matrix grain formations.

1. Introduction

Additive manufacturing (AM) has gained the attention of the aerospace industry for many years with its promises of reducing material waste, overall part costs, and production times [1–5]. AM is a process where parts are formed by depositing and joining material layer-by-layer as opposed to the traditional subtractive or formative manufacturing processes [6]. Based on ASTM standard, all metallic AM processes are classified into the following three categories: direct energy deposition, powder bed fusion, and sheet lamination [6]. Direct energy deposition requires either wire or powder feedstock material and an energy source, typically an electron beam [7], plasma arc [8], or laser [9].

Wire and arc additive manufacturing (WAAM) is a direct energy deposition process that uses wire feedstock and an electric arc as the energy source [10–12]. WAAM can be achieved with various energy sources including gas metal arc welding (GMAW) [2], gas tungsten arc welding (GTAW) [1], and plasma arc welding (PAW) [4]. There are several advantages to WAAM over other forms of metallic AM, such as the low capital costs associated with the machines and the flexibility in material compositions. WAAM systems can be built from commercially available components including a computer controlled robotic system, a welding power source, a welding torch, and a wire feed system. Low

capital cost makes WAAM a possible solution in large scale production as well as in small machine shops for manufacturing and repair purposes. Additionally, metal wires are cheaper, more readily available, and safer to handle than the metal powder alternative keeping the capital and operational costs low.

Wire-feed AM processes, including WAAM, provide a higher deposition rate than other forms of metallic additive manufacturing such as powder-based systems [10]. The increased deposition rate comes with a penalty in the form of reduced detail resolution and surface finish. Parts produced using WAAM typically require machining to obtain final dimensional tolerances and surface finishes. It has been shown that even with the additional machining step, WAAM remains more economical than entirely subtractive machining since there is less material waste [13]. In the aerospace industry, the ratio of material in the raw stock from to the final part is used to quantify the material waste during part production and is called the buy-to-fly ratio. A low buy-to-fly ratio is particularly advantageous in the aerospace industry for hard to machine and costly materials such as titanium. A comparative study of wire feeding and powder feeding AM machines was performed and concluded that both processes can yield similar microstructures and material properties, however some additional porosity was found in the powder feed samples [14].

A major challenge for all wire-feed AM processes comes from the

---

* Corresponding author.
  E-mail address: jeremy.laliberte@carleton.ca (J. Laliberte).

Fig. 1. WAAM machine.

Table 1
Nominal composition of HASTELLOY X alloy.

	Weight %
Nickel	47 (Balance)
Chromium	22
Iron	18
Molybdenum	9
Cobalt	1.5
Tungsten	0.6
Carbon	0.1
Manganese	1 (max)
Silicon	1 (max)
Boron	0.008 (max)
Niobium	0.5 (max)
Aluminum	0.5 (max)
Titanium	0.15 (max)

Table 2
Experimental factors and levels.

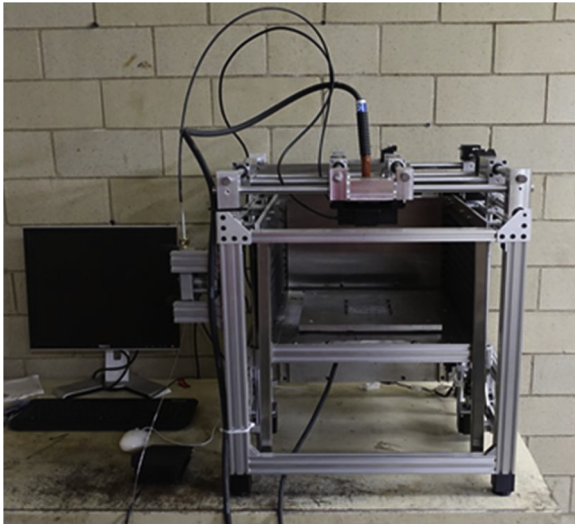|	Level			
Factor	1	2	3	4
A: Wire Feed Rate (mm/min)	200	230	260	290
B: Travel Speed (mm/min)	84	96	108	120
C: Current (A)	50	53	56	59
D: Argon Flow Rate (CFH)	20	25	30	35

residual stresses and distortion generated during the AM process. These phenomena are caused by the excessive energy input, high deposition rate, and large temperature gradient during the wire-feed AM processes. Therefore, one of the focuses of today's research is to understand and control the residual stresses and deformation caused when creating a part. In WAAM processes there are several key input factors that can be considered for determining optimal material characteristics. These include parameters such as travel speed, wire feed rate, working distance, arc voltage, and deposition strategy or path planning. This study considers the impact of some of these process parameters on the resultant specimen properties such as bead shape and size, bead roughness, and the microstructure.

2. Experimental procedure

All specimens were produced using a custom desktop sized Wire and Arc Additive Manufacturing (WAAM) machine developed at Carleton University, shown in Fig. 1. The motion of the welding torch along the horizontal plane as well as the vertical motion of the print bed are controlled by an onboard computer system. For this experiment, the WAAM machine was configured with a Miller Diversion 180 TIG welder as the power source and welding torch. Argon gas was used as a shielding gas and the flow rate was controlled manually with a flow valve at the tank reservoir. The feedstock delivery system consisted of an 80 W double drive 24 V wire feeder assembly originally intended for MIG welding. The welding torch is held in a vertical position with the wire feed entering from the side at a fixed angle.

All samples were created on top of a 1/8" thick 304 stainless-steel substrate, which was first prepared using a Canablast ECONOBLAST sandblasting unit to remove the surface contaminants. The welding wire selected for this study was HASTELLOY X alloy (Haynes International), a nickel-based alloy which possesses good oxidation resistance and high temperature performance [15]. The nominal composition of HASTELLOY X alloy is shown in Table 1. After deposition was completed, each specimen was immediately removed from the print bed, allowing each to cool to room temperature by a natural convection. After each specimen, the torch and print bed were cooled to ambient temperature to avoid variation between specimens.

A two-stage experiment was devised to study the effects of WAAM printing parameters. In the first stage, only a single layer of material is deposited onto the substrate to observe the effect on bead shape and quality. In the second stage, multiple layers are deposited with a focus on studying the interactions between layers.

For the first stage of the experiment, four factors were selected for

consideration; wire feed rate, travel speed, current, and argon flow rate. Each factor was given four levels, which are shown in Table 2. In order to consider all possible combinations, a full factorial experiment would require a total of 256 specimens. Therefore, to reduce the number of specimens in an efficient manner the Taguchi method was selected for this experiment. Since there are four four-level factors in this experiment, an L_{16} (4^4) orthogonal array was selected which can be seen in Table 3. This effectively reduces the total number of specimens required to 16.

The specimens were evaluated using multiple criteria to observe the resulting trends and effects. The following evaluation criteria were used to characterize weld quality; bead roughness, bead width, bead height, melt through depth, and wetting angle. A bead with a low surface roughness possesses no major height variations or waviness which is considered beneficial when depositing multiple weld beads on top of each other to maintain a relatively constant working distance and geometric accuracy. The bead width, bead height, melt through depth,

Table 3
Experimental L_{16} (4^4) orthogonal array.

	Level			
Sample #	A Wire Feed Rate	B Travel Speed	C Current	D Argon Flow Rate
B01	1	1	1	1
B02	1	2	2	2
B03	1	3	3	3
B04	1	4	4	4
B05	2	1	2	3
B06	2	2	1	4
B07	2	3	4	1
B08	2	4	3	2
B09	3	1	3	4
B10	3	2	4	3
B11	3	3	1	2
B12	3	4	2	1
B13	4	1	4	2
B14	4	2	3	1
B15	4	3	2	4
B16	4	4	1	3
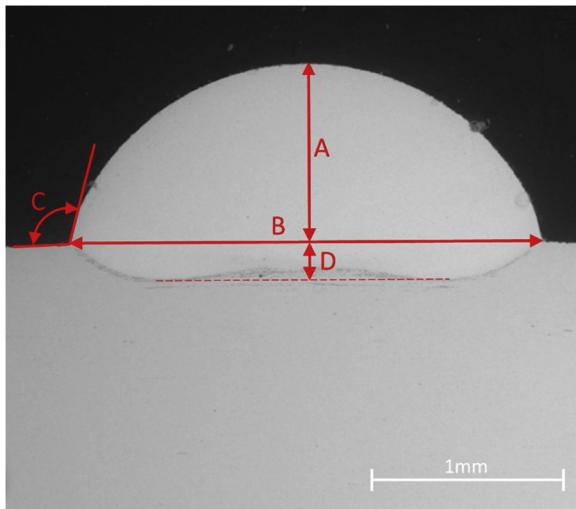
Fig. 2. Sample geometry measurements in SEM A) height, B) width, C) wetting angle, and C) melt through depth.

Fig. 3. Top view of single layer welds.

and wetting angle were measured to observe the effects of process parameters on the resulting geometry. The measurements were taken using ImageJ, an open source image processing software and are labeled in Fig. 2.

The bead roughness was measured using a Veeco Dektak 150 Profilometer. The specimens were cut using the Buehler Samplmet 2 abrasive cutter and mounted in a phenolic resin puck using a Buehler Simplimet II before being grinding and polishing. An SEM was used to obtain qualitative and quantitative observations including the melt through depth and wetting angle as well as observing the microstructure, porosity, and secondary phase formation in the bead.

For the second stage of the experiment, multiple-layered specimens were created to explore printing path strategies and observe the resulting geometry and microstructure. Printing path strategies included depositing consecutive layers of material in the same direction versus alternating directions, as well as controlling the reduction in heat input between consecutive layers.

Three additional samples (B41, B42, and B43) were created based on the findings of the preliminary trials. Their respective printing parameters can be seen in Table 4. The first layer of each specimen was printed using the parameters of sample B10 based on notable repeatability and several measured parameters detailed in this study. Samples B41 and B42 are made of four layers, each with alternating print directions and a 20% decrease in heat input between subsequent layers. Sample B43 consists of a total of eight layers with alternating print directions and a 20% decrease in heat input between layers for the first four layers. The heat input is held constant for the final four layers, as a steady state zone was found through trials, as discussed further in Section 3.2

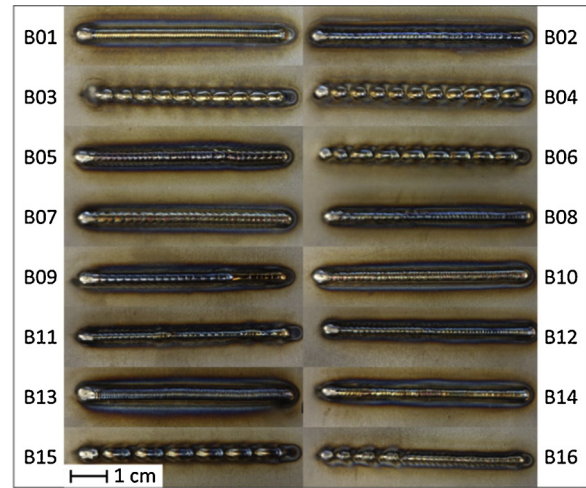After material deposition, the specimens were prepared in the same way as the first stage of the experiment for SEM observation, with an additional focus on the variation in secondary phase formation throughout the height of the bead.

3. Results and discussion

The results and discussion section is divided into two sections based on the two stages of the experiment, Sections 3.1 and 3.2.

3.1. First stage

This section will discuss the qualitative and quantitative results of the single layer specimens. All specimens from the first stage can be seen in Fig. 3 in a view perpendicular to the upper surface. Fig. 4 shows the beads at a low oblique angle to display the bead profiles.

Most of the specimens show signs of slight oxidation on the surface of the bead as well as in the heat affected zone of the substrate. The oxide layer formed mostly after the specimens were removed from the print bed and allowed to cool to room temperature through a natural convection without the presence of shielding gas or any other form of oxidation. The oxidation appeared as a blue or purple tint in most specimens (e.g. B05, B08, B13, etc.). As the oxide layer increases in thickness, the color transitions to a gold or straw color (e.g. B04, B07, B14, etc.).

There are four specimens (B03, B04, B06, and B15) which formed a discontinuous weld bead. In two of the cases, B03 and B04, the droplets remain separated whereas in specimens B06 and B15 the droplets are group in pairs. In all cases, the bead was not considered acceptable for AM applications due to their excessive height variations and discontinuities, therefore they were excluded from further evaluation.

The first evaluation criterion measured was bead roughness along the length of the bead. Profilometer data provided an arithmetic average roughness of the weld bead. Two measurements were made at different locations on each specimen which were averaged to produce a final value for evaluation purposes. A lower roughness value was considered desirable since there would be less variation in working distance during the deposition of subsequent layers.

Also using the SEM, the microstructure of the bead, the substrate, and the bead-substrate interface was observed in more detail as shown in Fig. 5.

Fig. 5 a) and b) show the columnar grain structure in the bead, nucleating from the bead-substrate interface (i.e., epitaxial growth [16]) and transitioning to a cellular grain arrangement higher in the bead. The columnar structure occurs since the substrate is not preheated and therefore a large temperature gradient is present at the

Table 4
Process parameters used for multi-layer samples (B41, B42, and B43).

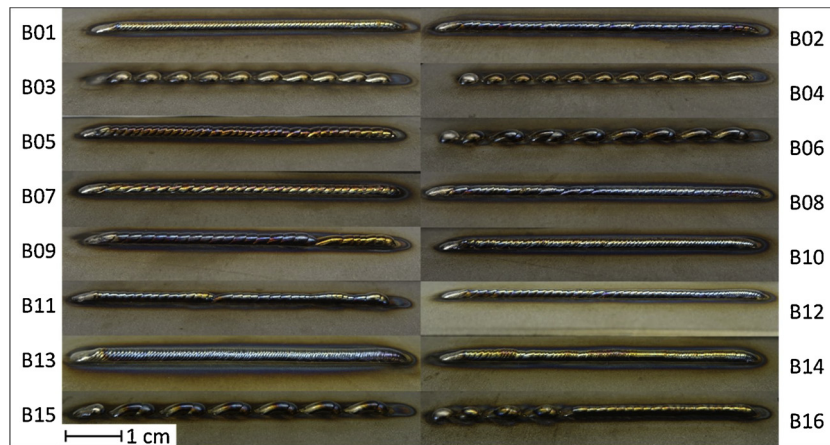| Layer	Travel Speed (mm/min)	Wire Feed Rate (mm/min)	Current (A)	Argon Flow Rate (CFH)
1	96	260	59	30
2	115.2			
3	138.2			
4	165.9			
5 (B43 Only)	165.9			
6 (B43 Only)	165.9			
7 (B43 Only)	165.9			
8 (B43 Only)	165.9			

Fig. 4. Low oblique angle view of single layer welds.

bead-substrate interface. Towards the top of the bead, the grains form a cellular arrangement since the temperature gradient is less significant and heat is transferred from the molten pool at a slower rate.

In both Figs. 2 and 5, it is noted that in the interface the center is raised slightly whereas the two edges penetrated deeper into the surface of the substrate. These geometrical features are referred to as 'humping' and 'undercutting'. 'Humping' and 'undercutting' can be caused by the fluid flow within the molten weld pool [17]. The suspected driving force behind the flow is that of the Marangoni effect, or more specifically the thermocapillary effect, where variations in surface tension cause the fluid flow [18].

The weld pool fluid flow may also be used to explain the presence of defects at the bead to substrate interface which can be seen more clearly in Fig. 6. The fluid flow in the bead circulated radially inwards at the

top causing a downward flow at the center of the bead to form. The interfacial defects were concentrated near the center of the bead suggesting that this flow may have swept gases towards the center of the bead during the solidification process.

For the purposes of AM, the substrate is often considered a consumable material which is removed. In cases where the substrate is part of the final part (such as in the application where details are created on a metal die using AM technology) efforts must be made to reduce the presence of these voids at the interface.

Energy-dispersive X-ray spectroscopy (EDS) analysis was performed to observe the compositional change across diffusion zone between the substrate and the bead. A color map is shown in Fig. 7, illustrating the concentration of several elements across the interface. Additionally, a quantitative scan was performed, yielding the graphs shown in Fig. 8.
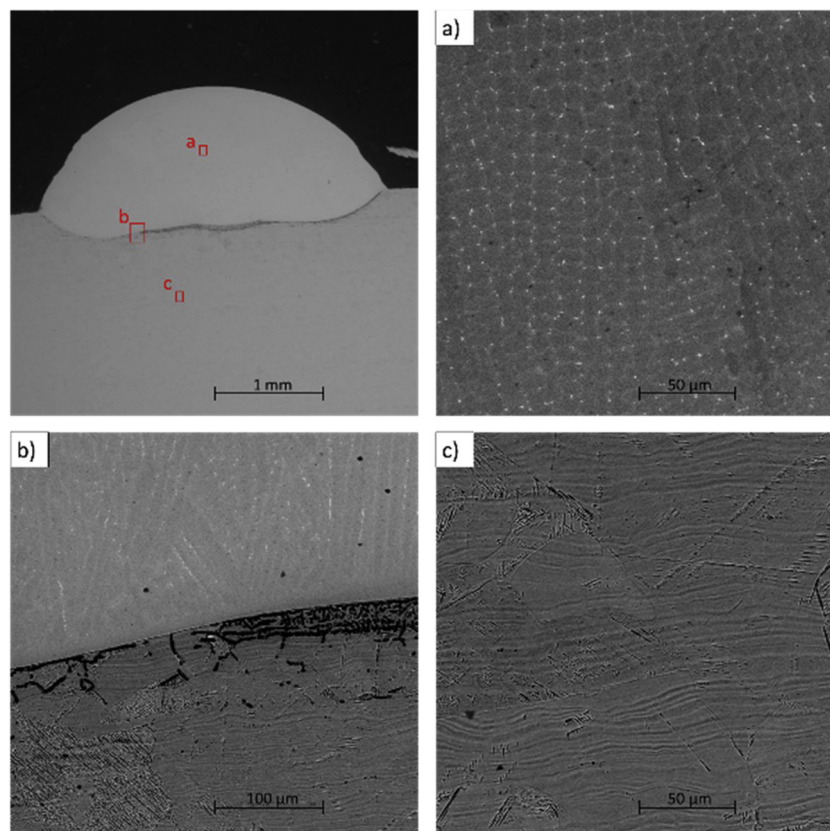

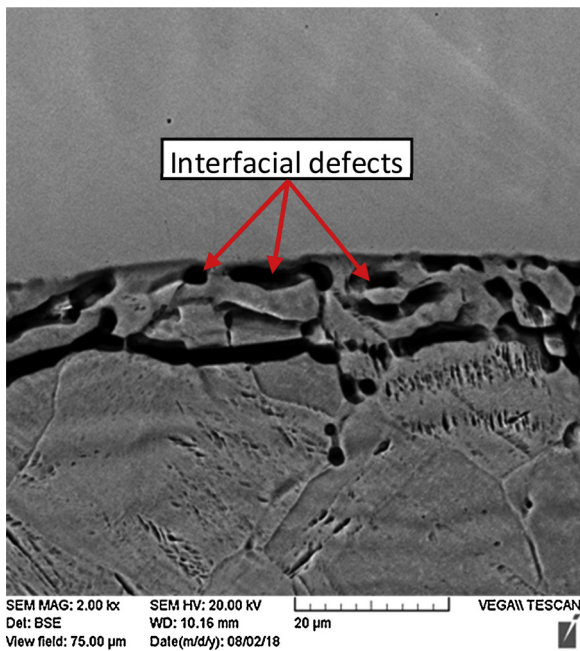**Fig. 5.** SEM images showing the microstructure of the bead and substrate (Sample B10).

Fig. 6. Voids at the bead-substrate interface (Bead shown on top).

The interface can be clearly identified in the graphs of elements such as iron, nickel, and molybdenum.

Finally, EDS was also used to identify the presence of carbides in the bead. By comparing the relative composition of carbon and molybdenum in the precipitates to that of the matrix the presence of molybdenum carbides can be confirmed. The carbides take the form of intragranular precipitates as labeled in Fig. 9.

The size and distribution of the carbide precipitates significantly change material properties such as strength and ductility [19]. Therefore, it is key to control their size and distribution throughout an additively manufactured part. The size and distribution of molybdenum carbides is discussed further in Section 3.2 where the carbides are monitored throughout the thickness of a four and an eight layered specimen.

3.1.1. Analysis of variance (ANOVA)

Statistical analysis was performed using Minitab 18 and selected interval plots are shown in Figs. 10 and 11. The first factor observed is the wire feed rate. The bead height increases in an approximately linear fashion as the wire feed rate increases and the bead width decreases only at the second feed rate. Since a higher wire feed rate results in a taller bead and narrower bead, the aspect ratio increases and the wetting angle decreases. Both the melt through depth and the roughness are considered independent of the wire feed rate.

The travel speed is considered next and in this case the bead width is shown to decrease with travel speed whereas the bead height does not vary significantly. This of course means that wetting angle decreases with travel speed. Unlike wire feed rate, the travel speed significantly impacts the melt through depth, which decreases as the travel speed increases.

Since the travel speed is increasing the heat input decreases and therefore the melt through depth is also expected to decrease. The bead roughness also shows a slight increase as the travel speed increases.

Since current and travel speed have an inverse effect on heat input, many of the trends are similar except with an inverse direction. Current shows the most significant impact on the bead roughness, with a small peak at the second level and then decreasing as current increases. The bead width is shown to increase with current and the bead height does not vary significantly. This results in an increase in wetting angle with current. Finally, the melt-through depth increases with an increase in current since the heat input is increased when other parameters are kept constant.

The argon flow rate was also considered during the ANOVA stage of the experiment, however, it resulted in no significant effects on the bead height, bead width, wetting angle, melt through depth, or roughness. This suggests that in future work, the argon flow rate does not need to be considered as a critical input variable and can be maintained at a constant level controlled by oxidation extent.

3.2. Second stage

This section will discuss the qualitative and quantitative results of the multiple layer specimens of stage two of the experiment. All specimens were created with the printing parameters of Sample B10, from stage 1, as the first layer since it yielded excellent results in all measured responses with repeatable results.

First, several printing strategies were tested by creating three-layer specimens as shown in Fig. 12. The difference between printing consecutive layers in the same direction versus alternating directions was explored. It has been envisioned that depositing all layers in the same direction can result in a high point at the end of the weld path and a low point at the beginning. Alternating print directions between layers was expected to reduce this effect. However, the specimens in Fig. 12 demonstrate that repeating the same print direction or alternating the print direction shows no significant difference in the bead shape for a three-layer specimen. This may not hold true for specimens with more layers as any small difference in height at the beginning or end of the bead will be magnified by each subsequent layer.

For the purposes of this experiment, no interpass pause time (hence cooling) was used. Instead, the heat input was reduced sequentially between each layer. Based on the findings of some preliminary trials, the heat input was decreased by either 5% or 20% between each layer.
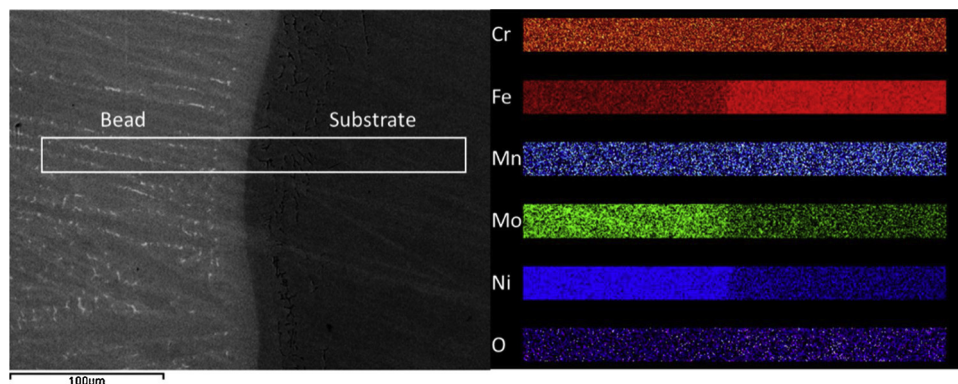

Fig. 7. Elemental scan results across bead-substrate interface (Bead shown on left).
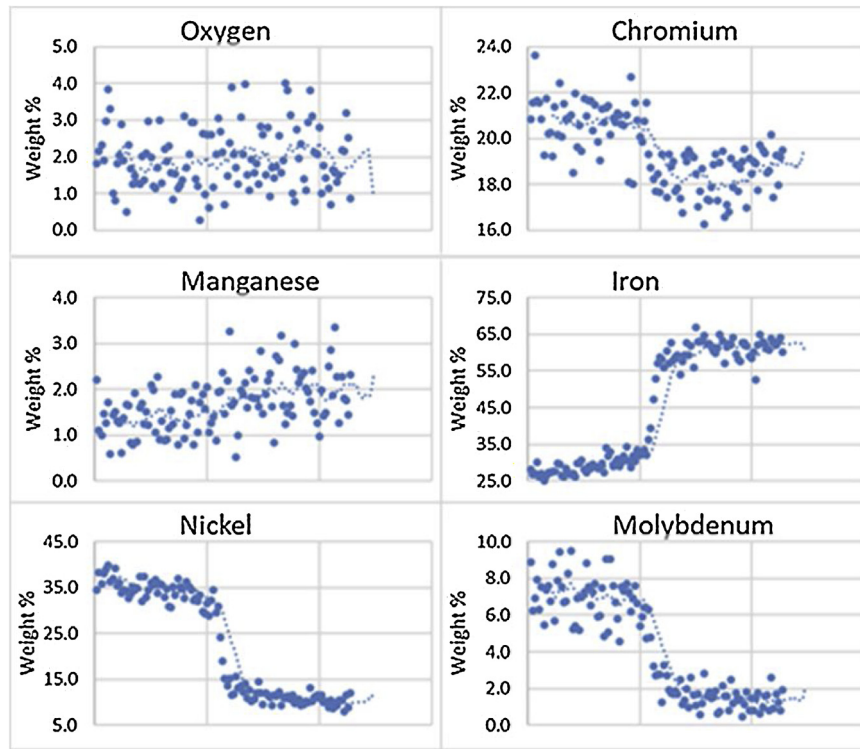
Fig. 8. Quantitative EDS analysis across bead-substrate interface (Oriented in same direction as labeled in Fig. 7).
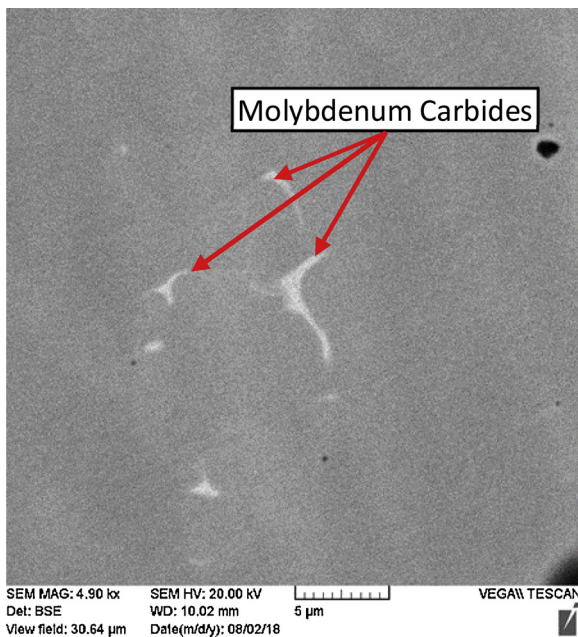

Fig. 9. Molybdenum carbide present in bead material.

The decrease in heat input was achieved by increasing the travel speed of each pass while maintaining a constant current. As seen in Fig. 12, no significant difference in bead shape, surface quality, or oxidation level can be seen between the samples with 5% reduction and 20% reduction. However, during the deposition of the third layers in the samples with 5% reduction, it was observed from the on-board camera that during the third pass both previous layers are completely remelted, indicating an excessive amount of heat input. Therefore, for further specimens it was decided to continue with a 20% decrease in heat input between each consecutive layer. This value will vary significantly based on the size and shape of the part to be printed and therefore to optimize

this value a thermodynamic study of the process would be required.

Contrary to the single layer specimen, the oxidation on the surface of the bead changes from a colourful blue or gold tint to a dull grey. This suggests a thicker oxide layer is forming on the surface of the bead. This change of color was also observed in all subsequent samples of multiple layers. Similarly, the oxide layer formed mostly after the specimens were removed from the print bed and allowed to cool through natural convection at room temperature.

As mentioned in the experimental procedure section, samples B41 and B42 (shown in Fig. 13) were created with four layers each using an alternating print direction and a 20% decrease in heat input each subsequent layer. Similar to before, the first layer of these specimens was created using the parameters of sample B10 and the parameters for each layer are shown in Table 4. It was noted that these printing parameters yielded excellent repeatability with almost no visible differences between samples B41 and B42. Next, sample B43 was created with a total of eight layers using alternating print directions and a 20% decrease in heat input between layers for the first four layers, after which a steady state was reached, and the heat input was held constant. The steady state zone was determined through trial and error testing where it was noted that further reduction in heat input resulted in extremely poor surface roughness or incomplete melting of the wire. All three samples can be seen in Fig. 13 with their respective cross sections.

Samples B41 and B42 have a very smooth bead profile with no variation in height at the beginning or the end of the bead. Sample 43 however has a rougher and more irregualr surface and a large buildup of material is present at both ends of the sample. This buildup is caused by the slight pause while the torch is raised between layers. During this vertical motion the arc is not stopped and therefore the wire continues to melt and is deposited at the end of the bead. This effect is compounded by each subsequent layer which explains its absence in the four-layer specimens. To prevent this from occurring in the future, the computer control will have to stop the arc or reduce the current temporarily while the torch is being raised for the subsequent layer.

The microstructre of the cross sections of specimens B41, B42, and B43 did not reveal any observable interface between the layers. This
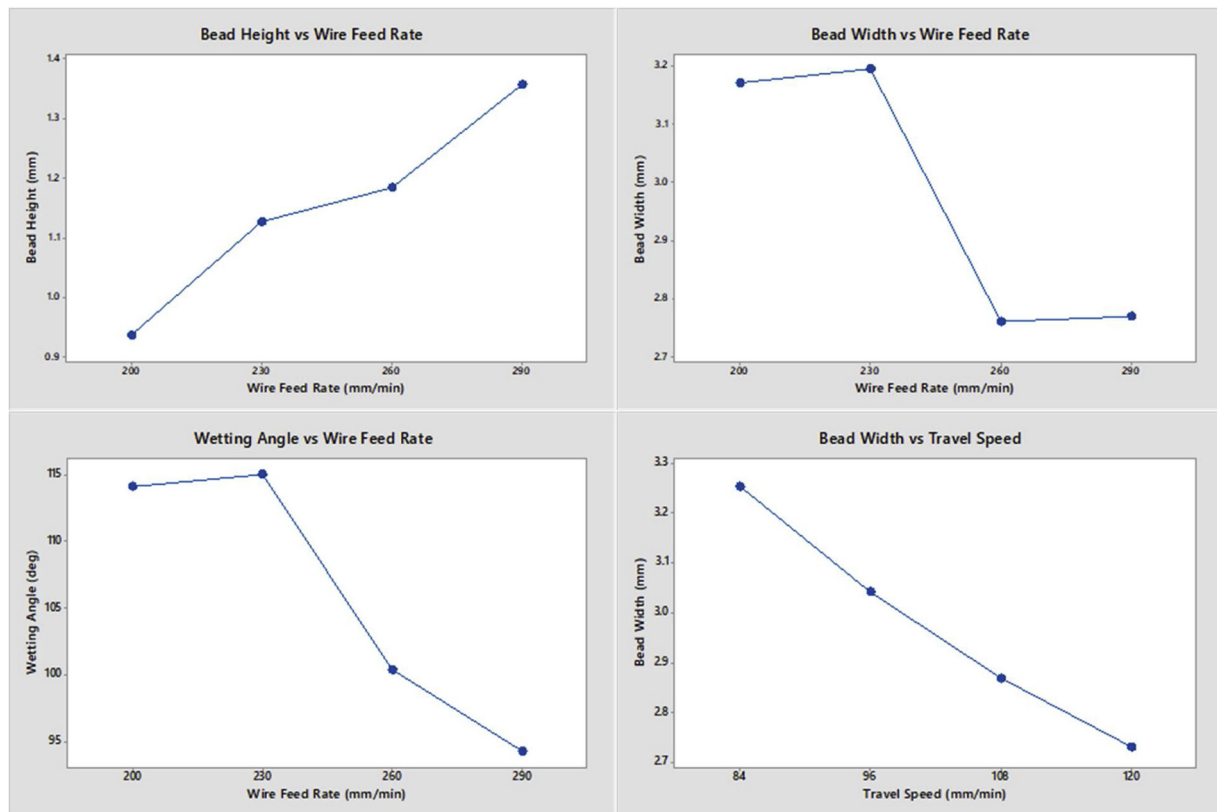
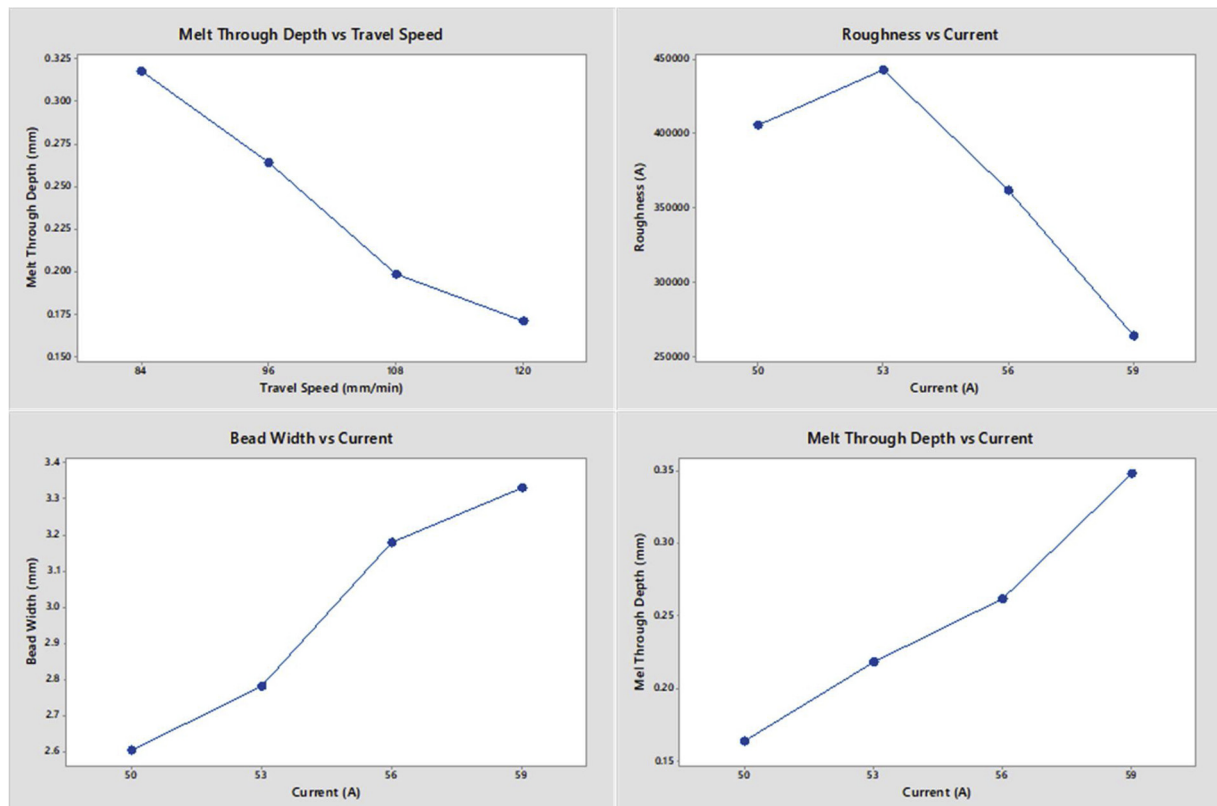**Fig. 10.** Interval plots displaying significant trends between factors and responses.

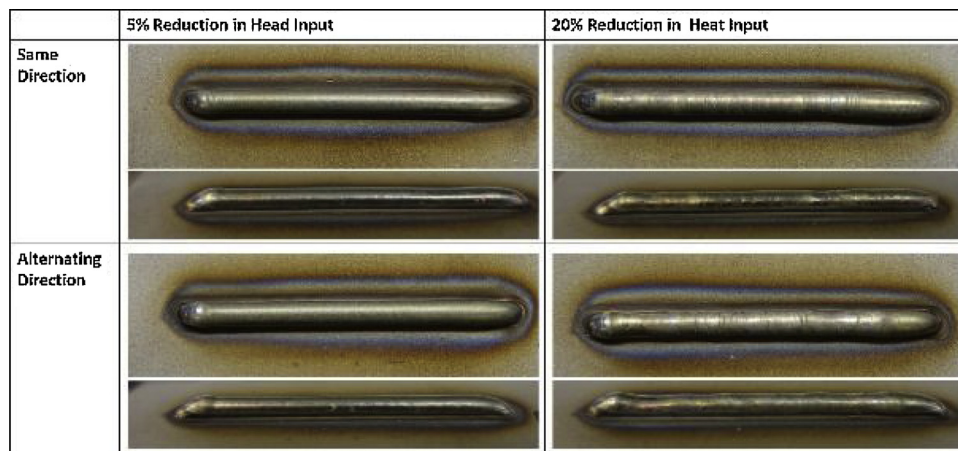**Fig. 11.** Interval plots displaying significant trends between factors and responses.

Fig. 12. Three layered specimens used to compare printing strategies. Each specimen shown in two views: top view (top) and low oblique angle view (bottom).
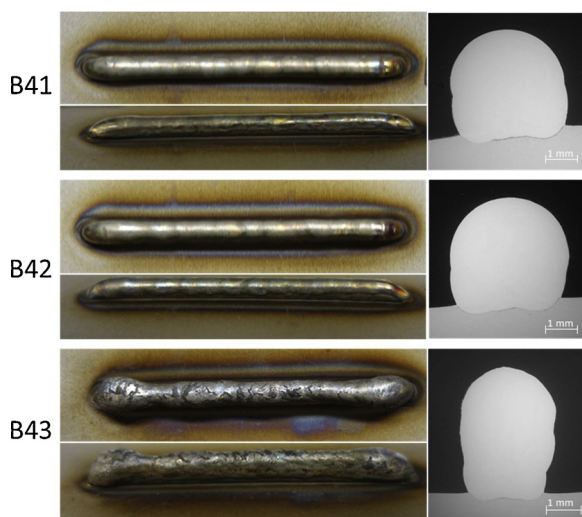

Fig. 13. Multiple layer specimens shown in two views with cross section on right.

suggests a complete fusion between layers with no oxidation present. Since no interpass pause time was used, the argon sheilding gas continued to flow between layers and effectively protected from oxidation. If an interpass pause time was used it is important to maintain the argon flow for oxidation prevention.

The size and shape of the molybdenum carbides varies significantly between layers suggesting that there is a significant difference in thermal history between layers (Fig. 14). Three distinct zones were observed. First, nearest to the bead-substrate interface, the carbides are finer and evenly distributed amongst the columnar grain matrix. This first zone is shown in Fig. 14 a). The second zone is seen in Fig. 14 b), c), and d) where the carbides grow larger and reduce in number. This is due to the subsequent reheating when next layer of material is deposited, resulting in a relatively slow cooling rate for carbide growth. The third and final zone is seen at the top of the bead (Fig. 14 e). The carbides return to a fine and even distribution except now distributed amongst a cellular grain formation. The small and evenly distributed carbide formations in the first zone is caused by the large temperature difference between the cold substrate and the molten wire material. The thermal gradient cools the molten metal before the carbides grow. Similarly, in the third zone, the molten metal is cooled quickly through convection and is remelted since no subsequent layer are added.

Depending on the application and the desired material strength, ductility, and hardness, post additive manufacture heat treatment may be required. The printing strategies presented in this section results in large and non-uniformly distributed carbides throughout the majority of the specimen. To optimize the microstructure, a post additive manufacturing heat treatment may be used to redistribute the carbides and restore the material properties.

4. Conclusions

This paper presents a study on the effects of process parameters in TIG based WAAM and the finding can be summarized as follows.

- Due to the fluid flow during the weld pool solidification 'humping' and 'undercutting' were observed in the substrate as well as a concentration of interfacial defects at the center of the bead-substrate interface.
- The presence of molybdenum carbides was confirmed using EDS analysis.
- One-way ANOVA was performed to determine trends between each factor and response. Significant trends were observed, including:
  ○ Bead height increases linearly with wire feed rate. Both melt through depth and roughness are independent of wire feed rate.
  ○ Bead width decreases with travel speed. Melt through depth decreases significantly with travel speed.
  ○ Travel speed and current inversely affect heat input and therefore show similar trends except in opposite direction. Increasing travel speed or decreasing current causes a decrease in melt through depth and an increase in roughness.
  ○ Argon flow rate resulted in no significant effects on the bead height, bead width, wetting angle, melt through depth, or roughness, suggesting that the argon flow rate can be maintained at a constant level controlled by oxidation extent during future work.
- Printing path strategies were tested using three layered specimens. No significant difference was found between printing layers in the same direction or in alternating direction. Additionally, in lieu of an interpass pause, a 20% decrease in heat input between layers was determined to be acceptable to yield a uniform deposition.
- In all specimens of multiple layers, no observable interface between the layers was present suggesting a complete fusion between layers with no oxidation.
- Three distinct zones were identified within the multiple layer samples. In the first zone, nearest to the bead-substrate interface, the carbides are fine and evenly distributed amongst the columnar grain matrix. The second zone includes larger and less evenly distributed carbides. Finally, in the third zone, the carbides return to a fine and evenly distributed arrangement within a cellular grain structure.
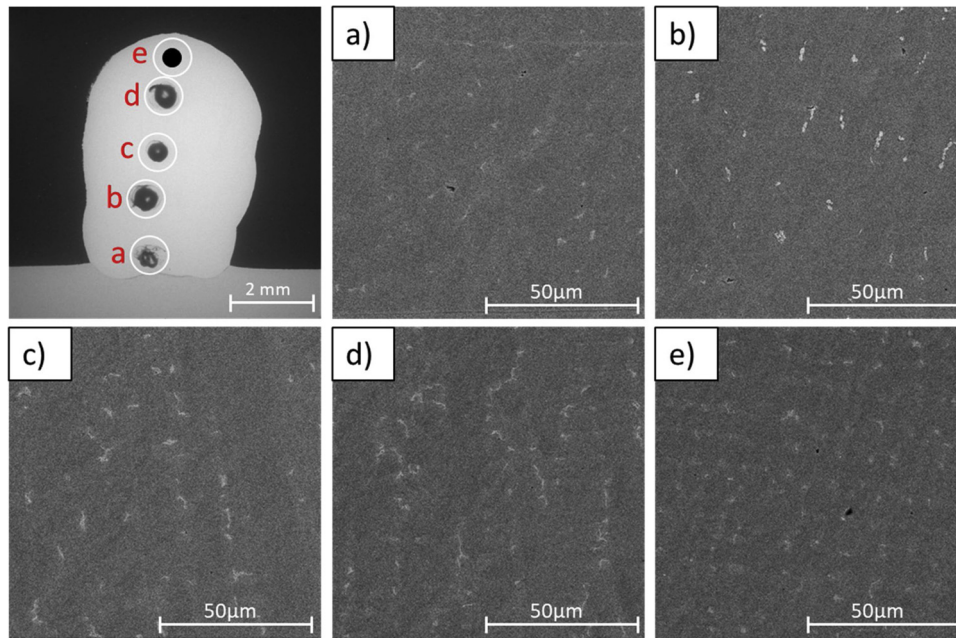
Fig. 14. Microstructure of specimen B41 from bottom to top of cross section.

References

[1] A.A. Antonysamy, Microstructure, Texture and Mechanical Property Evolution During Additive Manufacturing Of Ti6Al4V Alloy for Aerospace Applications, The University of Manchester, 2012.

[2] A.S. Haselhuhn, Design for Low-Cost Gas Metal Arc Weld-Based Aluminum 3-D Printing, Michigan Technological University, 2016.

[3] E.R. Denlinger, Thermo-Mechanical Model Development and Experimentalvalidation for Metallic Parts in Additive Manufacturing, The Pennsylvania State University, 2015.

[4] J.N. Stavinoha, Investigation of Plasma Arc Welding as a Method for the Additive Manufacturing of Ti-6Al-4V Alloy Components, Montana Tech of The University of Montana, 2012.

[5] X. Qiu, Effect of Rolling on Fatigue Crack Growth Rate of Wire and Arc Additive Manufacture (WAAM) Processed Titanium, Cranfield University, 2013.

[6] A. 52900, Standard terminology for additive manufacturing – General principles – terminology, ASTM Int. i (2015) 1–9 2015.

[7] A. Adebayo, Characterisation of Integrated WAAM and Machining Processes, Cranfield University, 2013.

[8] P.M.S. ALMEIDA, Process Control and Development in Wire and Arc Additive Manufacturing, (2012).

[9] Y. Ding, M. Akbari, R. Kovacevic, Process planning for laser wire-feed metal additive manufacturing system, Int. J. Adv. Manuf. Technol. 95 (1–4) (2018) 355–365.

[10] D. Ding, Z. Pan, D. Cuiuri, H. Li, Wire-feed additive manufacturing of metal components: technologies, developments and future interests, Int. J. Adv. Manuf. Technol. 81 (1–4) (2015) 465–481.

[11] A. Busachi, J. Erkoyuncu, P. Colegrove, F. Martina, J. Ding, Designing a WAAM based manufacturing system for defence applications, CIRP 37 (2015) 48–53.

[12] S.W. Williams, F. Martina, A.C. Addison, J. Ding, G. Pardal, P. Colegrove, Wire + arc additive manufacturing, Mater. Sci. Technol. 32 (7) (2016) 641–647.

[13] Y. Zhai, Early Cost Estimation for Additive Manufacture, Cranfield University, 2012.

[14] W.U.H. Syed, A.J. Pinkerton, L. Li, A comparative study of wire feeding and powder feeding in direct diode laser deposition for rapid prototyping, Appl. Surf. Sci. 247 (1–4) (2005) 268–276.

[15] Haynes International, HASTELLOY ® X Alloy, [Online]. Available: (2017) . [Accessed: 02-Jun-2018] http://www.haynesintl.com/alloys/alloy-portfolio_/High-temperature-Alloys/HASTELLOY-X-alloy/HASTELLOY-X-principal-features.aspx.

[16] A.S.M. International, Weld solidification, in: S. Lampman (Ed.), Weld Integrity and Performance, ASM International, Novelty, Ohio, 1997, p. 19.

[17] K.C. Mills, B.J. Keene, R.F. Brooks, A. Shirali, Marangoni effects in welding, Philos. Trans. R. Soc. A Math. Phys. Eng. Sci. 356 (1739) (1998) 911–925.

[18] C.R. Heiple, J.R. Roper, Mechanism for minor element effect on GTA fusion zone geometry, Weld. J. 61 (4) (1982) 97–102.

[19] D. Tomus, Y. Tian, P.A. Rometsch, M. Heilmaier, X. Wu, Influence of post heat treatments on anisotropy of mechanical behaviour and microstructure of Hastelloy-X parts produced by selective laser melting, Mater. Sci. Eng. A 667 (2016) 42–53.